Chapter

# Wakefield Excitation in Carbon Nanotubes: An Extended Hydrodynamic Model

*Pablo Martín-Luna and Javier Resta-López*


## Abstract

As charged particles traverse carbon nanotubes, they can trigger collective oscillations within the electron gas trapped inside the graphene-based cylindrical structures that form the nanotube walls. Such collective modes, referred to as plasmonic excitations, have garnered significant attention as a feasible mechanism for enabling particle acceleration across sub-millimeter scales with exceptionally high field gradients. This innovative concept could significantly transform acceleration technologies, paving the way for groundbreaking advancements across high-energy physics and its allied disciplines. In this work, we use an extended hydrodynamic model that, in contrast to conventional formulations, incorporates distinct restoring frequencies for $\sigma$ and $\pi$ electrons, thereby capturing the harmonic binding-induced restoring forces acting on the electron fluid displacement. This approach provides a more realistic description of the collective electron behaviour, as it yields dispersion relations that closely resemble those obtained experimentally. Analytical expressions for the induced longitudinal and transverse wakefields are obtained, revealing their intrinsic link to the resonant modes governed by the system's dispersion characteristics. The impact of critical model variables, including particle speed, nanotube radius, and friction coefficient on the wakefields, is examined, comparing these findings with those from the conventional hydrodynamic model.


**Keywords:** carbon nanotubes (CNTs), extended hydrodynamic model, wakefield excitation, nanomaterials, plasmonics, particle acceleration, restoring frequencies

## 1. Introduction

Particle accelerators constitute essential infrastructure for the advancement of scientific research, driving industrial innovation, and contributing to economic growth. Conventional accelerators rely on radiofrequency (RF) technologies and are constrained to accelerating gradients around 100 MV/m due to the limiting effects of surface RF breakdown [1, 2]. Various alternative approaches are actively being explored to exceed this limitation, including dielectric laser accelerators and wakefield acceleration schemes [3–7], as well as plasma-based acceleration techniques [8–12]. Notably, during the 1980s and 1990s, Tajima and collaborators proposed solid-state wakefield acceleration employing crystals as a promising avenue for achieving acceleration gradients in the TV/m regime [13–15]. In the original conceptual framework introduced by Tajima [13], longitudinal wakefields are generated by high-energy ($\approx$40 keV) X-ray photons injected into the crystal lattice at the Bragg angle, thereby inducing the Borrmann–Campbell effect [16, 17]. Likewise, ultrashort pulses of charged particles can excite electric wakefields throughout the crystalline structure, facilitating efficient energy transfer from the primary (driver) bunch to a strategically placed secondary (witness) bunch. Nevertheless, the intrinsic limitations associated with angstrom-scale channel dimensions in natural crystals restrict beam intensity acceptance and lead to elevated dechannelling rates.

Owing to their hollow cylindrical geometry, carbon nanotubes (CNTs) can facilitate the channelling and steering of charged particles in a manner analogous to conventional crystal channelling. Empirical demonstrations have verified the transport of 2 MeV $He^{+}$ ions [18] and 300 keV electrons [19] through CNTs. Compared to natural crystals, CNTs offer wider channels in two dimensions and longer dechannelling lengths [20, 21], which position them as promising candidates for sustaining TV/m-level acceleration gradients. This is further supported by their remarkable electronic characteristics, enhanced structural adaptability, and superior thermo-mechanical stability. Consequently, carbon-based nanomaterials (including CNTs and graphene layers) are actively being investigated as novel media to sustain particle wakefield acceleration [22–31].

Surface-localized collective oscillations of the delocalized electron gas in CNTs, widely designated as surface plasmons, can act as a driving mechanism for the generation of wakefields within these nanomaterials. Wakefield formation stems from the dynamic interplay between a relativistic driver bunch and the CNT interface. Theoretical investigations into the electronic excitations on single- and multi-walled CNTs have employed a wide range of modeling frameworks, including dielectric theory [32–34], hydrodynamic models [35–38], two-fluid models [39, 40], quantum hydrodynamic models [41], kinetic theories [42–45], and hybrid approaches combining semi-classical kinetic formulations with molecular dynamics simulations [46].

In this chapter, we have employed an extension of the linearized hydrodynamic model (LHM) that incorporates restoring frequencies, which render the dispersion relations more consistent with experimental measurements [47]. We have derived analytical expressions for the excited wakefields, which have been related to the resonant frequencies and compared with the results obtained previously (which use one- and two-fluid models without restoring frequencies). The LHM has been selected because of its simplicity, its good agreement with the dielectric formalism in the random-phase approximation [36], and its capability to explain the modifications inflicted on single-walled CNTs (SWCNTs) irradiated with swift heavy ions [48].

This chapter is divided into the following sections. Section 2 presents a comprehensive introduction to the LHM, detailing the general analytical expressions for both longitudinal and transverse wakefields generated by a charged particle as it travels paraxially through a SWCNT. Section 3 delivers an in-depth exploration of the dispersion relation, the behaviour of the induced wakefields, and the energy dissipation (stopping power) across varying particle velocities and CNT radii, with a comparative assessment of the one-fluid and two-fluid theoretical models. Unless stated otherwise, atomic units are employed throughout the chapter. Section 4 offers a concise synthesis of the principal findings derived from this study.

## 2. Theoretical framework

We start by reviewing the hydrodynamic model, which will be applied to describe excitations occurring on the surface of a SWCNT of radius $a$, resulting from the motion of a charged particle in its vicinity. Within this theoretical framework, the CNT is represented as an idealized cylindrical shell, infinitely thin and extending indefinitely in length. The delocalized electrons associated with carbon ions are modeled as a two-dimensional Fermi gas (essentially a free-electron system) restricted to the cylindrical surface of the nanotube. Within the two-fluid framework, this electron population is partitioned into two separate components: one representing the $\sigma$ electrons and the other corresponding to the $\pi$ electrons. The initial uniform surface density for these fluids is $n_{0\sigma} = 0.75n_g$ and $n_{0\pi} = 0.25n_g$ ($n_g = 4 \times 0.107$) is the electron-gas density of a graphite sheet assuming four free electrons per carbon ion [36, 49]), corresponding to three $\sigma$ electrons and one $\pi$ electron per carbon atom, respectively. In the one-fluid model, no distinction is made between $\sigma$ and $\pi$ electrons, so only a single fluid with surface density $n_0 = n_g$ is considered. We consider a point-like charged particle $Q$ travelling at a constant velocity $v$ parallel to the CNT axis, as illustrated in **Figure 1**. If energy dissipation is neglected, the position of the charged particle in cylindrical coordinates as a function of time $t$ is given by $\mathbf{r}_0(t) = (r_0, \varphi_0, vt)$. This moving charge induces a perturbation of the electrons within the CNT wall, which are modeled as charged fluids characterized by a surface density $n(\mathbf{r}_a, t) = n_{0j} + n_j(\mathbf{r}_a, t)$ and velocity fields $\mathbf{u}_j(\mathbf{r}_a, t)$. Here, $j = \{\pi, \sigma\}$, and $\mathbf{r}_a = (a, \varphi, z)$ denotes the cylindrical coordinates of an arbitrary point on the surface of the CNT, while $n_j(\mathbf{r}_a, t)$ represents the perturbed electron density per unit area for each fluid component. In the LHM, the fluid velocities $\mathbf{u}_j$ and the perturbed densities $n_j$ are treated as small perturbations. Furthermore, the radial component of the velocity fields vanishes, since the electron gas is confined to the cylindrical surface of the CNT. When studying wakefield dynamics, it is reasonable to ignore ionic motion [50, 51], since its associated time scale is orders of magnitude longer than that of electronic motion due to the significantly greater mass of carbon ions compared to electrons.

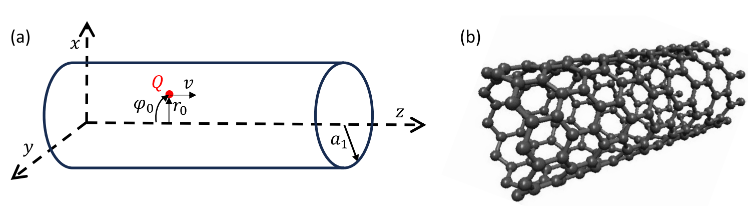


**Figure 1.**
*(a) Schematic representation of a point-like charge Q travelling parallel to the z-axis inside a CNT. (b) Illustration of the hexagonal lattice structure characteristic of a CNT.*

Electronic excitations on the nanotube surface are governed by the continuity equation:

$$\frac{\partial n_j(\mathbf{r}_a,t)}{\partial t} + n_{0j} \quad {}_{\parallel} \cdot \mathbf{u}_j(\mathbf{r}_a,t) = 0, \quad j = \pi, \sigma, \tag{1}$$

as well as the non-relativistic momentum balance equation governing the electron fluid on each nanotube wall:

$$\frac{\partial \mathbf{u}_j\,(\mathbf{r}_a,t)}{\partial t} = \quad {}_{\parallel}\Phi(\mathbf{r}_a,t) - \frac{\alpha_j}{n_{0j}} \quad {}_{\parallel} n_j(\mathbf{r}_a,t) + \frac{\beta}{n_{0j}} \quad {}_{\parallel}\left[\ {}^{2}_{\parallel} n_j(\mathbf{r}_a,t)\right] - \gamma_j \mathbf{u}_j(\mathbf{r}_a,t), \quad j = \pi, \sigma, \tag{2}$$

where only first-order terms in $n_j$ and $\mathbf{u}_j$ have been retained. Here, $\mathbf{r} = (r, \varphi, z)$ denotes the position vector, $\Phi$ the electric scalar potential, and $\quad = \hat{\mathbf{r}}\,\frac{\partial}{\partial r} + \hat{\boldsymbol{\varphi}}\,\frac{1}{r}\frac{\partial}{\partial \varphi} + \hat{\mathbf{z}}\,\frac{\partial}{\partial z}$, ${}_{\parallel} = \hat{\boldsymbol{\varphi}}\,\frac{1}{a}\frac{\partial}{\partial \varphi} + \hat{\mathbf{z}}\,\frac{\partial}{\partial z}$. Eq. (2) comprises four distinct terms. The first term on the right-hand side represents the force exerted by the tangential electric field on the electrons located on the surface of the $j$-th nanotube. The overall electrostatic potential, which satisfies the three-dimensional Poisson equation in vacuum, is decomposed as $\Phi = \Phi_0 + \Phi_{\text{ind}}$. Here, $\Phi_0 = \frac{Q}{\|\mathbf{r}-\mathbf{r}_0\|}$ represents the Coulomb potential originating from the external driving charge, while $\Phi_{\text{ind}}$ accounts for the potential generated by the perturbations in the electron fluid system, which can be calculated as:

$$\Phi_{\text{ind}}(\mathbf{r},t) = -\sum_{j=\pi,\,\sigma}\int \mathrm{d}^2\mathbf{r}'\,\frac{n_j\left(\mathbf{r}',t\right)}{\|\mathbf{r}-\mathbf{r}'\|}, \tag{3}$$

where $\mathbf{r}' = (a, \varphi', z')$ and $\mathrm{d}^2\mathbf{r}' = a\,\mathrm{d}\varphi'\mathrm{d}z'$. The second term captures the coupling to acoustic excitation modes, parameterized by $\alpha_j = v_{F_j}^2/2$, where the Fermi velocity of the two-dimensional electron gas is given by $v_{F_j} = \sqrt{2\pi n_{0j}}$. In contrast, the third term, where $\beta = \frac{1}{4}$, arises from the functional derivative of the von Weizsäcker gradient correction to the equilibrium kinetic energy density, reflecting single-electron quantum effects in the fluid dynamics of the electron gas [52]. The final term represents a dissipative force acting on the electrons, arising from their scattering with the stationary ionic background. Alternatively, this damping term, characterized by the coefficient $\gamma_j$, can be interpreted phenomenologically to model plasmon resonance broadening in the excitation spectrum of diverse material systems [32].

Eqs. (1)–(3) admit an analytical treatment via the application of the Fourier–Bessel (FB) transform. Specifically, the FB transform $\widetilde{f}(m,k,\omega)$ of a generic function $f(\varphi,z,t)$ is defined as follows:

$$f(\varphi,z,t) = \sum_{m=-\infty}^{\infty}\int_{-\infty}^{\infty}\frac{\mathrm{d}k}{(2\pi)^2}\int_{-\infty}^{\infty}\frac{\mathrm{d}\omega}{2\pi}\,\mathrm{e}^{ikz+im\varphi-i\omega t}\widetilde{f}(m,k,\omega). \tag{4}$$

The Coulomb potential can be represented as

$$\frac{1}{\|\mathbf{r}-\mathbf{r}'\|} = \sum_{m=-\infty}^{\infty}\int_{-\infty}^{\infty}\frac{\mathrm{d}k}{(2\pi)^2}\,\mathrm{e}^{ik(z-z')+im(\varphi-\varphi')}g(r,r';m,k), \tag{5}$$

where $g(r, r'; m, k) \equiv 4\pi I_m(|k| r_{\min}) K_m(|k| r_{\max})$ with $r_{\min} = \min(r, r')$, $r_{\max} = \max(r, r')$, and $I_m(x)$ and $K_m(x)$ denoting the modified Bessel functions of the first and second kind, respectively, of integer order $m$. Substituting the expression given in Eq. (5) into Eq. (3), the FB transform of $\Phi_{\text{ind}}$ is obtained as:

$$\widetilde{\Phi}_{\text{ind}}(r, m, k, \omega) = -\sum_{j=\pi,\sigma} g(r, a; m, k) a \widetilde{n}_j(m, k, \omega), \tag{6}$$

where $\widetilde{n}_j$ stands for the FB transform of the perturbed charge density $n_j$. By applying the continuity equation to express the velocity field $\mathbf{u}_j$ in terms of the perturbed density in Eq. (2), and using the definition of the FB transform, one obtains a system of $N$ coupled linear equations whose solution yields the transformed perturbation densities:

$$S_j(m, k, \omega)\widetilde{n}_j(m, k, \omega) - \sum_{l=\pi,\sigma} G_{jl}(m, k)\widetilde{n}_l(m, k, \omega) = B_j(m, k, \omega),\ j = \pi, \sigma, \tag{7}$$

where we have defined:

$$S_j(m, k, \omega) = \omega(\omega + i\gamma_j) - \alpha_j\left(k^2 + m^2/a^2\right) - \beta\left(k^2 + m^2/a^2\right)^2, \tag{8}$$

$$G_{jl}(m, k) = 4\pi n_{0j} a\left(k^2 + m^2/a^2\right) I_m(|k|a) K_m(|k|a), \tag{9}$$

$$B_j(m, k, \omega) = -n_{0j}\left(k^2 + m^2/a^2\right)\widetilde{\Phi}_0(a, m, k, \omega). \tag{10}$$

In Eq. (10), $\widetilde{\Phi}_0$ denotes the FB transform of the Coulomb potential created by the driving particle:

$$\widetilde{\Phi}_0(r, m, k, \omega) = 2\pi Q\, g\,(r, r_0; m, k)\, \delta\,(\omega - kv) e^{-im\varphi_0}, \tag{11}$$

with $\delta$ denoting the Dirac delta function. It is noteworthy that Eq. (7) can be reformulated as the following matrix equation:

$$M\vec{\widetilde{n}} = \vec{B},\ M_{jj} = S_j - G_{jj},\ M_{ij} = -G_{ij}\ (i \neq j). \tag{12}$$

Accordingly, the resonant frequencies associated with the collective excitations in the coupled electron fluids arise as solutions to the eigenvalue problem: $det(M) = 0$ under the condition $\gamma_j = 0$.

The longitudinal and transverse components of the induced electric wakefield are respectively described by

$$\begin{aligned} W_{z,\text{ind}} = -\frac{\partial \Phi_{\text{ind}}}{\partial z} &= \frac{1}{(2\pi)^3} \sum_{m=-\infty}^{+\infty} e^{im\varphi} \int_{-\infty}^{+\infty} \mathrm{d}k\, k \Big( \mathrm{Re}[\widetilde{\Phi}_{\text{ind}}(r, m, k, kv)\Big] \sin(k\zeta) \\ &\quad + \mathrm{Im}[\widetilde{\Phi}_{\text{ind}}(r, m, k, kv)]\, \cos(k\zeta)) = W_{z,\,\text{Re}} + W_{z,\text{Im}}, \end{aligned} \tag{13}$$

$$\begin{aligned} W_{r,\text{ind}} = -\frac{\partial \Phi_{\text{ind}}}{\partial r} &= -\frac{1}{(2\pi)^3} \sum_{m=-\infty}^{+\infty} e^{im\varphi} \int_{-\infty}^{+\infty} \mathrm{d}k\, \Big( \mathrm{Re}[\partial_r \widetilde{\Phi}_{\text{ind}}(r, m, k, kv)\Big] \cos(k\zeta) \\ &\quad - \mathrm{Im}[\partial_r \widetilde{\Phi}_{\text{ind}}(r, m, k, kv)]\, \sin(k\zeta)) = W_{r,\,\text{Re}} + W_{r,\text{Im}}. \end{aligned} \tag{14}$$

These expressions rely on the definition of the comoving coordinate $\zeta = z - vt$, along with the symmetry properties of the FB transform,

$\mathrm{Re}[\widetilde{f}(k,kv)] = \mathrm{Re}[\widetilde{f}(-k,\,-kv)]$, $\mathrm{Im}[\widetilde{f}(k,kv)] = -\mathrm{Im}[\widetilde{f}(-k,\,-kv)]$ for the functions $\widetilde{f}(k,kv) = \left\{\widetilde{\Phi}_{\mathrm{ind}}(r,m,k,kv), \partial_r\widetilde{\Phi}_{\mathrm{ind}}(r,m,k,kv)\right\}$.

Eqs. (13) and (14) have been decomposed into two distinct contributions, arising from the real and imaginary parts of $\widetilde{\Phi}_{\mathrm{ind}}$. In practical computations, an upper cutoff must be imposed on the longitudinal wavenumber $k$ to limit the integration domain. This numerical constraint not only accelerates the evaluation but also mitigates the emergence of artifacts associated with high-frequency modes. The quantities $W_{z,\mathrm{Im}}$ and $W_{r,\mathrm{Im}}$ can be analytically calculated if $\gamma_j \to 0^+$. Now, let's proceed to analyze the result in the context of each of the three models under consideration: the one-fluid model, the two-fluid model, and the two-fluid model incorporating restoring frequencies (i.e., the extended hydrodynamic model).

### 2.1 One-fluid model

In this model, no distinction is made between $\pi$ and $\sigma$ electrons; consequently, the subscript $j$ in the equations of the LHM model refers to the single fluid under consideration, and the homogeneous surface density is given by $n_0 = n_g$. In this case, the dispersion relations (the solutions to the eigenvalue equation: $\det(M) = 0$ for $\gamma = 0$), are given by:

$$\omega_m^2(k) = \alpha\left(k^2 + m^2/a^2\right) + \beta\left(k^2 + m^2/a^2\right)^2 + \Omega_p^2 a^2\left(k^2 + m^2/a^2\right)K_m(|k|a)I_m(|k|a) \quad (15)$$

where $\Omega_p = \sqrt{4\pi n_0/a}$ is the plasma frequency. Furthermore, if $\gamma \to 0^+$, the quantities $W_{z,\,\mathrm{Im}}$ and $W_{r,\,\mathrm{Im}}$ can be analytically calculated as follows [23, 26]:

$$W_{z,\mathrm{Im}}(r,\varphi,\zeta) = \sum_{m=-\infty}^{+\infty} e^{im\varphi} W_{z,\,m}\cos(k_m\zeta), \quad W_{r,\mathrm{Im}}(r,\varphi,\zeta) = \sum_{m=-\infty}^{+\infty} e^{im\varphi} W_{r,\,m}\sin(k_m\zeta), \quad (16)$$

with

$$W_{z,\,m} = \frac{-Q}{8\pi^2} e^{-im\varphi_0} k_m \Omega_p^2 a^2\left(k_m^2 + m^2/a^2\right) g\left(a, r_0; m, k_m\right) g\left(a, r; m, k_m\right) \left|\frac{\partial Z_m}{\partial k}\right|_{k=k_m}^{-1}, \quad (17)$$

$$W_{r,\,m} = \frac{-Q}{8\pi^2} e^{-im\varphi_0} \Omega_p^2 a^2\left(k_m^2 + m^2/a^2\right) g\left(a, r_0; m, k_m\right) \partial_r g\left(a, r; m, k_m\right) \left|\frac{\partial Z_m}{\partial k}\right|_{k=k_m}^{-1}. \quad (18)$$

where $Z_m(k) = (kv)^2 - \omega_m^2(k)$ and $k_m$ are the positive roots of $Z_m(k)$, which is the condition for plasma resonance $k_m v = \omega_m(k_m)$.

### 2.2 Two-fluid model

In this case, the plasmon dispersion relations are given by:

$$\omega_\pm^2(m,k) = \frac{\omega_\pi^2 + \omega_\sigma^2}{2} \pm \sqrt{\left(\frac{\omega_\pi^2 - \omega_\sigma^2}{2}\right)^2 + \Delta^2}, \quad (19)$$

where

$$\omega_j^2 = \alpha_j\left(k^2 + m^2/a^2\right) + \beta\left(k^2 + m^2/a^2\right)^2 + 4\pi n_{0j}a\left(k^2 + m^2/a^2\right)I_m(|k|a)K_m(|k|a) \quad (20)$$

are the dispersion relations corresponding to the individual electron fluids $j = \pi, \sigma$, and

$$\Delta^2 = (4\pi)^2 n_{0\pi} n_{0\sigma} a^2\left(k^2 + m^2/a^2\right)^2\left(I_m(|k|a)K_m(|k|a)\right)^2 \quad (21)$$

originates from the electrostatic coupling between the two electron fluids.

Similarly, the terms $W_{z,\mathrm{Im}}$ and $W_{r,\mathrm{Im}}$ can be analytically integrated if $\gamma_j \to 0^+$ [25, 29]:

$$W_{z,\mathrm{Im}}(r,\varphi,\zeta) = \sum_{m=-\infty}^{+\infty} e^{im\varphi}\left[W_{z,m}^{+}\cos(k_m^{+}\zeta) + W_{z,m}^{-}\cos(k_m^{-}\zeta)\right], \quad (22)$$

$$W_{r,\mathrm{Im}}(r,\varphi,\zeta) = \sum_{m=-\infty}^{+\infty} e^{im\varphi}\left[W_{r,m}^{+}\sin(k_m^{+}\zeta) + W_{r,m}^{-}\sin(k_m^{-}\zeta)\right], \quad (23)$$

$$W_{z,m}^{+} = \frac{k_m^{+}}{(2\pi)^2}\left(Z_m^{-}(k_m^{+}, k_m^{+}v)\left|\frac{\partial Z_m^{+}}{\partial k}\right|_{k=k_m^{+}}\right)^{-1}\sum_{j=\pi,\sigma} g\left(r,a;m,k_m^{+}\right)aN_j(m,k_m^{+},k_m^{+}v), \quad (24)$$

$$W_{z,m}^{-} = \frac{k_m^{-}}{(2\pi)^2}\left(Z_m^{+}(k_m^{-}, k_m^{-}v)\left|\frac{\partial Z_m^{-}}{\partial k}\right|_{k=k_m^{-}}\right)^{-1}\sum_{j=\pi,\sigma} g\left(r,a;m,k_m^{-}\right)aN_j(m,k_m^{-},k_m^{-}v), \quad (25)$$

$$W_{r,m}^{+} = \frac{1}{(2\pi)^2}\left(Z_m^{-}(k_m^{+}, k_m^{+}v)\left|\frac{\partial Z_m^{+}}{\partial k}\right|_{k=k_m^{+}}\right)^{-1}\sum_{j=\pi,\sigma} \partial_r g\left(r,a;m,k_m^{+}\right)aN_j(m,k_m^{+},k_m^{+}v), \quad (26)$$

$$W_{r,m}^{-} = \frac{1}{(2\pi)^2}\left(Z_m^{+}(k_m^{-}, k_m^{-}v)\left|\frac{\partial Z_m^{-}}{\partial k}\right|_{k=k_m^{-}}\right)^{-1}\sum_{j=\pi,\sigma} \partial_r g\left(r,a;m,k_m^{-}\right)aN_j(m,k_m^{-},k_m^{-}v), \quad (27)$$

where $k_m^{\pm}$ are the positive roots of $Z_m^{\pm}(k) = (kv)^2 - \omega_{\pm}^2(m,k)$ and we have defined the auxiliary functions

$$N_\pi(m,k,\omega) = (S_\sigma - G_{\sigma\sigma})B_\pi' + G_{\pi\sigma}B_\sigma',\; N_\sigma(m,k,\omega) = (S_\pi - G_{\pi\pi})B_\sigma' + G_{\sigma\pi}B_\pi', \quad (28)$$

where $B_j'$ denote the functions $B_j$ with the Dirac delta term $\delta(\omega - kv)$ removed, that is,

$$B_j'(m,k)\delta(\omega - kv) = B_j(m,k,\omega),\; j = \pi, \sigma. \quad (29)$$

### 2.3 Extended model: Two-fluid model with restoring frequencies

Earlier one- and two-fluid approaches suggest that plasmon frequencies vanish as the wave vector $k$ approaches zero (cf. Eqs. (15) and (19), and **Figure 2**). This result contradicts the experimental fact that $\pi$- and $(\sigma + \pi)$-plasmons in a SWCNT approach finite frequencies in the limit $k \to 0$ [53]. For this reason, a realistic

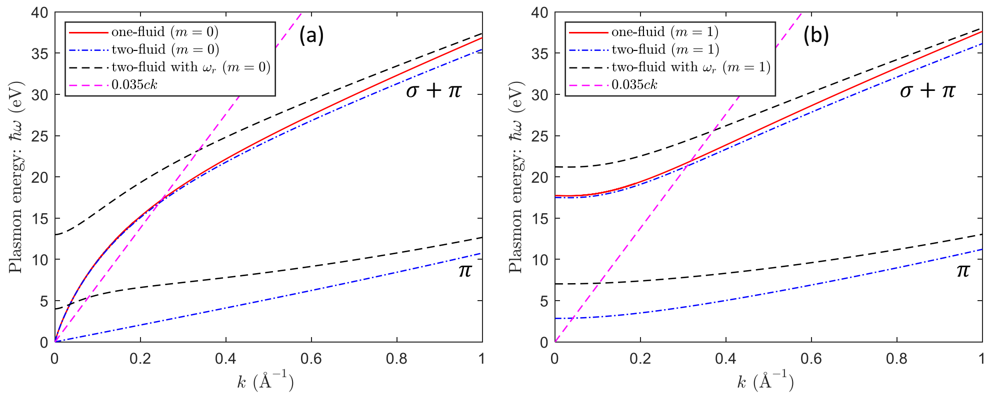


**Figure 2.**
*Plasmon dispersion relations $\omega_m(k)$ for a CNT with $a = 0.36$ nm, using the one-fluid model, the two-fluid model, and the two-fluid extended model with $\omega_{r\pi} = 4$ eV and $\omega_{r\sigma} = 13$ eV. Panel (a) presents the fundamental mode ($m = 0$), while panel (b) displays the first azimuthal mode ($m = 1$). The resonant wavenumbers $k_m$ correspond to the intersection points between the dispersion curves $\omega_m(k)$ and the line defined by kv, plotted for a driving velocity of $v = 0.0.35c$.*

approach involves incorporating restoring frequencies for the $\pi$ and $\sigma$ electron fluids (they will be denoted as $\omega_{r\pi}$ and $\omega_{r\sigma}$, respectively), which account for the restoring forces acting on fluid displacements arising from electron binding, modeled within the harmonic approximation framework. We will use the numerical values $\omega_{r\pi} = 4$ eV and $\omega_{r\sigma} = 13$ eV, which are based on electron energy loss spectroscopy (EELS) measurements [47, 54]. These frequencies may be related to the interband transitions $\pi \to \pi^+$ and $\sigma \to \sigma^+$ [47]. To incorporate these restoring effects into the LHM framework, it is sufficient to include the restoring frequencies directly in the definition of the auxiliary function $S_j$ [47, 53]:

$$S_j(m,k,\omega) = \omega(\omega + i\gamma_j) - \omega_{rj}^2 - \alpha_j\left(k^2 + m^2/a^2\right) - \beta\left(k^2 + m^2/a^2\right)^2, j = \pi, \sigma. \tag{30}$$

Consequently, the dispersion relations and the analytical expressions for $W_{z,\mathrm{Im}}$ and $W_{r,\mathrm{Im}}$ in this model are formally identical to those of the two-fluid model, with the key distinction that the characteristic frequencies $\omega_j$ are now defined as:

$$\omega_j^2 = \omega_{rj}^2 + \alpha_j\left(k^2 + m^2/a^2\right) + \beta\left(k^2 + m^2/a^2\right)^2 + 4\pi n_{0j} a\left(k^2 + m^2/a^2\right) I_m(|k|a) K_m(|k|a), \tag{31}$$

which will evidently lead to significant modifications in the numerical results.

## 3. Results and discussion

This section explores the wakefields generated by a point charge traversing the interior of a CNT, with a comparative analysis of outcomes derived from the one-fluid, two-fluid, and the extended two-fluid model, the latter accounting for restoring frequency effects. As inferred from Eqs. (16)–(18) and (22)–(27), the resonant wavenumbers $k_m$ and $k_m^{\pm}$, which arise from the plasma resonance condition, play a crucial role in characterizing the wakefield behaviour. Accordingly, the discussion starts with a comprehensive examination of the dispersion relation.

### 3.1 Dispersion relations

**Figure 2** illustrates the dispersion profiles $\omega_m(k)$ corresponding to the fundamental mode ($m = 0$) and the first azimuthal mode ($m = 1$) for a CNT with a radius $a = 0.36$ nm. In the one-fluid model, a single dispersion curve corresponds to each azimuthal mode $m$. For the two-fluid models, the dispersion curve splits into two distinct dispersion relations $\omega_\pm(k)$; in particular, the upper branch in the two-fluid model without restoring frequencies resembles the dispersion curve from the one-fluid model, while the lower branch can be approximated as follows [29, 39]:

$$\omega_-(0,k) \approx kv_p,\, v_p = \sqrt{\frac{2\pi n_{0\pi} n_{0\sigma}}{n_{0\pi} + n_{0\sigma}}}. \tag{32}$$

The key distinction introduced by incorporating restoring frequencies into the two-fluid model of a CNT emerges at short wavenumbers $k$ in the fundamental mode $m = 0$: whereas in models without restoring frequencies, the dispersion relations tend to zero at $k \to 0$, the dispersion relations asymptotically approach finite values ($\omega_{r\pi}$ and $\omega_{r\sigma}$, respectively) if the restoring frequencies are considered. These finite values are better aligned with the experimental excitation of $\pi$- and $(\sigma + \pi)$-plasmons [38].

**Figure 2** also shows the $kv$-line whose intersection with each dispersion curve indicates the resonant frequency $k_m$. In general, for the two-fluid model lacking restoring frequencies, only the upper dispersion curve of the fundamental plasmonic mode ($m = 0$) is excited, except when the velocity of the driving particle approaches $v_p$ (cf. Eq. (32)), since, when this occurs, the resonant wavenumber corresponding to the lower dispersion curve of the two-fluid model can be excited. However, when introducing the restoring frequencies, two resonant wavenumbers can be excited for any azimuthal mode $m$ (one for each dispersion relation), except at very low driving velocities where the $kv$-line does not intercept the dispersion relations.

### 3.2 Induced electric wakefields

To streamline the analytical treatment, and unless stated otherwise, the following analysis adopts a uniform damping coefficient, $\gamma \equiv \gamma_j$, for both fluids ($\sigma$ and $\pi$ electrons) and assumes a positively charged ion ($Q = 1$), which may represent a proton, as the particle inducing the wakefields.

**Figure 3** illustrates the respective roles of the real and imaginary components of $\widetilde{\Phi}_{\text{ind}}$ to the induced longitudinal wakefield for a driving velocity of $v = 0.035c$ in a CNT with a radius $a = 0.36$ nm, comparing the results obtained using the two-fluid model with and without the restoring frequencies. A small value of the damping parameter has been adopted to enable a comparison with the result derived from the resonant wavenumbers, Eq. (22), since the frictional parameter $\gamma$ leads to an exponential attenuation of the induced wakefield with increasing distance behind the driving particle (cf. **Figure 5**). Furthermore, when restoring frequencies are incorporated into the two-fluid model, two distinct modes are excited (albeit one with low amplitude and thus barely perceptible), resulting in a shorter wavelength compared to the two-fluid model without restoring frequencies, in which only a single resonant wavenumber is excited. Moreover, it is observed that $W_{z,\text{Re}}$ and $W_{z,\text{Im}}$ exhibit nearly identical profiles, with noticeable differences only in the immediate vicinity of the driving particle. Therefore, when the damping parameter $\gamma$

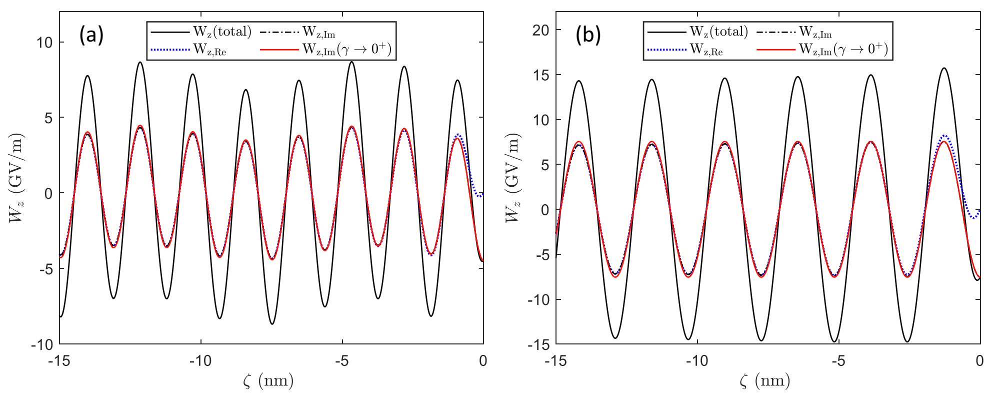


**Figure 3.**
*Longitudinal wakefield contributions along the axis ($r = 0$) induced by a positively charged ion ($Q = 1$) travelling on axis ($r_0 = 0$), assuming a damping parameter $\gamma = 10^{-3}\Omega_p$ with $\Omega_p = \sqrt{4\pi n_g / a}$, a CNT radius $a = 0.36$ nm and a driving velocity $v = 0.035c$. In (a), we show the wakefields obtained using the two-fluid extended model with $\omega_{r\pi} = 4$ eV and $\omega_{r\sigma} = 13$ eV; and in (b), the two-fluid model. The red curves correspond to the limiting case $\gamma \to 0^+$: Eq. (22). The driving particle is located at $\zeta = 0$.*

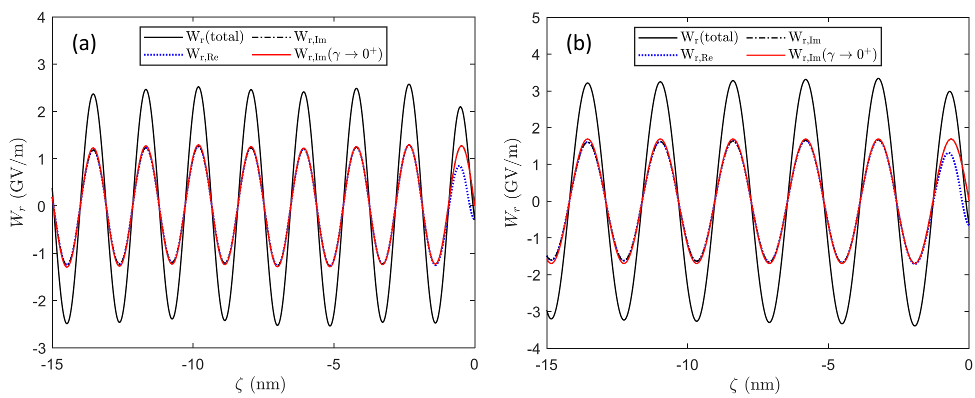


**Figure 4.**
*Transverse wakefield contributions along $r = a/2$ induced by a positively charged ion ($Q = 1$) travelling on axis ($r_0 = 0$), assuming a damping parameter $\gamma = 10^{-3}\Omega_p$ with $\Omega_p = \sqrt{4\pi n_g / a}$, a CNT radius $a = 0.36$ nm, and a driving velocity $v = 0.035c$. In (a), we show the wakefields obtained using the two-fluid extended model with $\omega_{r\pi} = 4$ eV and $\omega_{r\sigma} = 13$ eV; and in (b), the two-fluid model. The red curves correspond to the limiting case $\gamma \to 0^+$: Eq. (23). The driving particle is located at $\zeta = 0$.*

is small, the induced longitudinal wakefield can be well approximated as $W_z \approx 2W_{z,\mathrm{Im}}$, where $W_{z,\mathrm{Im}}$ is determined using Eq. (22).

Similarly, **Figure 4** depicts the induced transverse wakefield along $r = a/2$ for the same parameters as those in **Figure 3**, exhibiting similar behaviour. For this reason, the induced transverse wakefield can be estimated as $W_r \approx 2W_{r,\mathrm{Im}}$, where $W_{r,\mathrm{Im}}$ is determined using Eq. (23).

For completeness, **Figure 5** presents both the longitudinal and transverse wakefields computed using the two-fluid extended model with realistic values of the damping parameter, illustrating the exponential decay of the fields behind the driver.

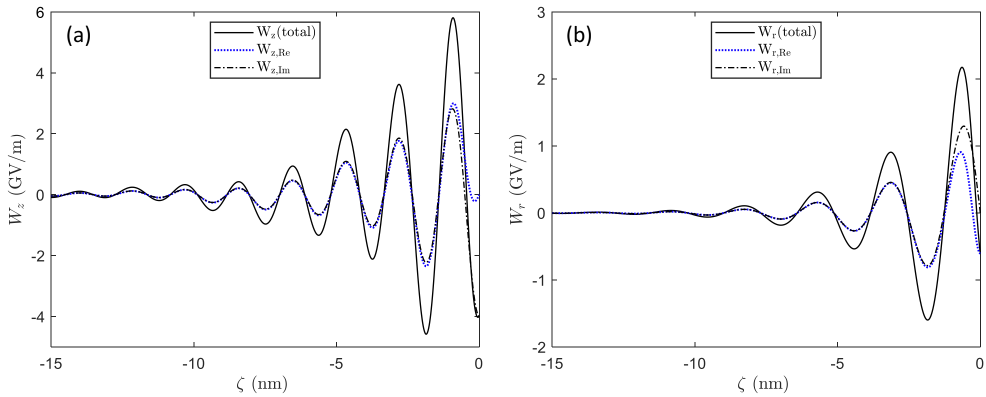


**Figure 5.**
*(a) Longitudinal wakefield along the z-axis and (b) transverse wakefield along $r = a/2$ induced by a positively charged ion ($Q = 1$) travelling with velocity $v = 0.035c$ on axis ($r_0 = 0$) within a CNT with radius $a = 0.36$ nm for the two-fluid extended model with realistic values of the restoring frequencies and damping parameters: $\omega_{r\pi} = 4$ eV, $\omega_{r\sigma} = 13$ eV, $\gamma_\pi = 0.09 = 2.45$ eV, and $\gamma_\sigma = 0.10 = 2.72$ eV [47, 54]. The driving particle is located at $\zeta = 0$.*

On the contrary, **Figures 6** and **7** display the induced longitudinal and transverse wakefields, respectively, for a CNT with radius $a = 1$ nm. In this case, a more intricate wakefield pattern appears when restoring frequencies are taken into account, owing to the fact that the two excited modes exhibit comparable amplitudes. Therefore, given the relevance of the amplitude associated with the excited modes, the following section focuses on its analysis.

Finally, the perturbed densities for each electron fluid are depicted in **Figure 8**. In this case, when the restoring frequencies are neglected, $n_\pi/n_{0\pi}$ and $n_\sigma/n_{0\sigma}$ are almost identical. This result explains the close agreement between the one-fluid and two-fluid models; for this reason, the induced wakefields calculated with the one-fluid

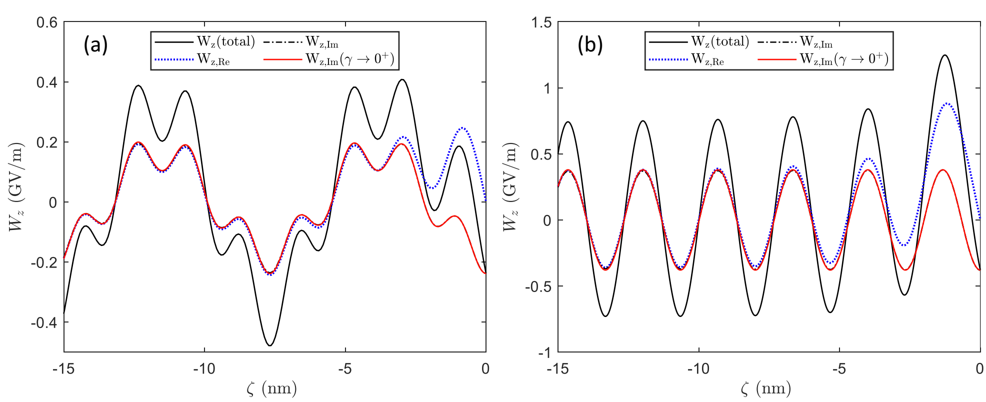


**Figure 6.**
*Longitudinal wakefield contributions along the axis ($r = 0$) induced by a positively charged ion ($Q = 1$) travelling on axis ($r_0 = 0$), assuming a damping parameter $\gamma = 10^{-3}\Omega_p$ with $\Omega_p = \sqrt{4\pi n_g/a}$, a CNT radius $a = 1$ nm, and a driving velocity $v = 0.035c$. In (a), we show the wakefields obtained using the two-fluid extended model with $\omega_{r\pi} = 4$ eV and $\omega_{r\sigma} = 13$ eV; and in (b), the two-fluid model. The red curves correspond to the limiting case $\gamma \to 0^+$: Eq. (22). The driving particle is located at $\zeta = 0$.*

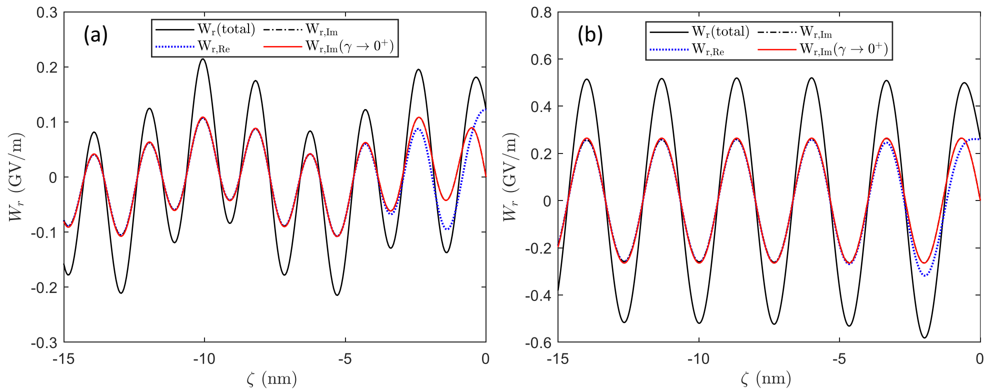


**Figure 7.**
*Transverse wakefield contributions along $r = a/2$ induced by a positively charged ion ($Q = 1$) travelling on axis ($r_0 = 0$), assuming a damping parameter $\gamma = 10^{-3}\Omega_p$ with $\Omega_p = \sqrt{4\pi n_g/a}$, a CNT radius $a = 1$ nm, and a driving velocity $v = 0.035c$. In (a), we show the wakefields obtained using the two-fluid extended model with $\omega_{r\pi} = 4$ eV and $\omega_{r\sigma} = 13$ eV; and in (b), the two-fluid model. The red curves correspond to the limiting case $\gamma \to 0^+$: Eq. (23). The driving particle is located at $\zeta = 0$.*

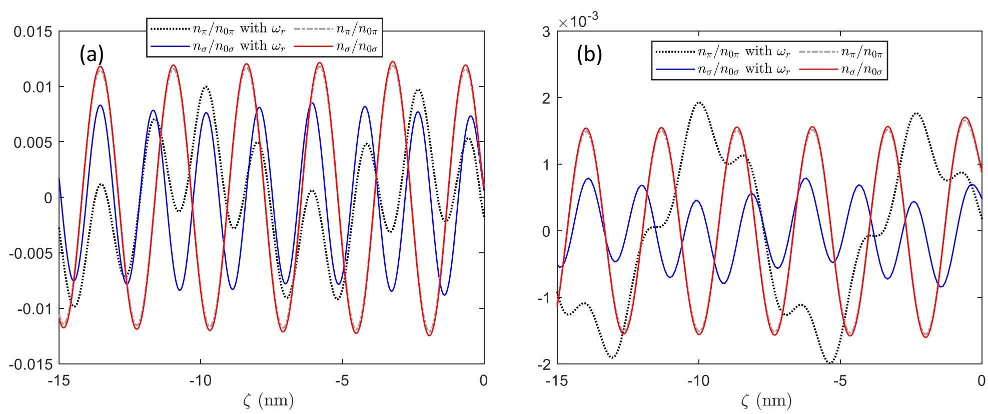


**Figure 8.**
*Perturbed densities for a positively charged ion ($Q = 1$) travelling on axis ($r_0 = 0$) with a velocity $v = 0.035c$ and $\gamma = 10^{-3}\Omega_p$ for (a) $a = 0.36$ nm and (b) $a = 1$ nm. In both cases, we compare the perturbed densities obtained using the two-fluid extended model with $\omega_{r\pi} = 4$ eV and $\omega_{r\sigma} = 13$ eV and the two-fluid model. The driving particle is located at $\zeta = 0$.*

model have not been shown in this section. It is worth noting that the condition $n_j \ll n_{0j}$ is satisfied, as required by the LHM.

### 3.3 Excited modes: Amplitude and resonant wavenumbers

As it has been established in the preceding section, when the damping parameter satisfies $\gamma_j \to 0^+$, plasmonic excitations can be approximated by $2W_{z,\mathrm{Im}}$. This section focuses on the specific case of an on-axis plasmonic excitation induced by a positively charged ion ($Q = 1$) travelling along the CNT axis ($r = r_0 = 0$), which implies $W_r = 0$ and restricts the excitation to the zero-order angular-momentum mode, $m = 0$. **Figure 9** presents a comparison of the absolute values of the excited modes (negative in the case

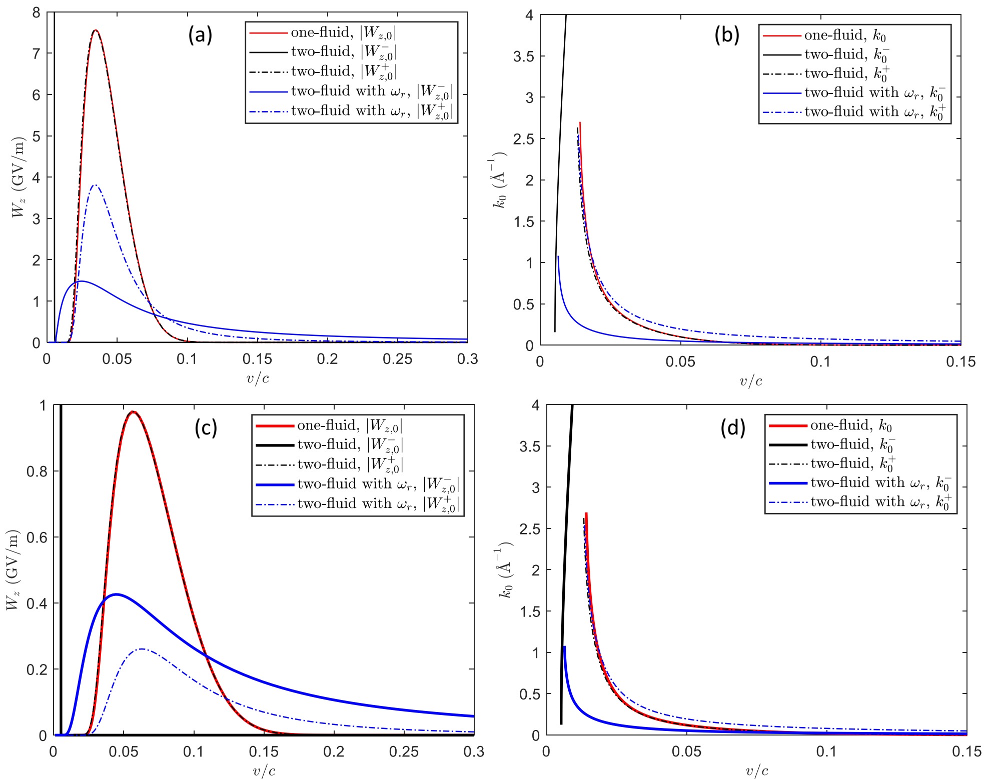


**Figure 9.**
*(a) Amplitudes $W_z$ of the fundamental mode $m = 0$ and (b) corresponding resonant wavenumbers $k_0$ as functions of the driving particle velocity for a CNT, computed using the one-fluid model, the standard two-fluid model, and the two-fluid model with restoring frequencies with $\omega_{r\pi} = 4$ eV and $\omega_{r\sigma} = 13$ eV for $a = 0.36$ nm. (c) and (d) are identical to (a) and (b), respectively, but for $a = 1$ nm. A value of $r = r_0 = 0$ is considered in all plots.*

of $Q = 1$) and their corresponding resonant wavenumbers $k_0$ as functions of the particle velocity for CNTs with radii $a = 0.36$ nm and $a = 1$ nm, respectively. It can be observed that the only mode that can be excited in the one-fluid model resembles the mode associated with the upper dispersion relation of the two-fluid model without restoring frequencies. The mode associated with the lower branch of the dispersion relation in the two-fluid model without restoring frequencies is only appreciable for velocities $v = v_p$, as previously examined in literature [29]. Conversely, the inclusion of restoring frequencies in the two-fluid model enables the excitation of both modal branches associated with each azimuthal mode $m$, with the exception of regimes involving very low driving velocities. These modes exhibit greater amplitudes at high velocities compared to models that do not account for restoring frequencies.

Furthermore, **Figure 10** illustrates how the amplitude of the excited modes varies with the CNT radius. It is observed that the one-fluid and two-fluid models without restoring frequencies yield practically identical results, revealing an optimal radius at which the intensity of the excited fields reaches its maximum. This optimal radius increases with the velocity of the driving particle. Regarding the two-fluid model incorporating restoring frequencies, the amplitude of the mode with the lowest resonant wavenumber decreases as the CNT radius increases, while the amplitude of the other mode also exhibits a peak, similar to the models without the restoring frequencies.

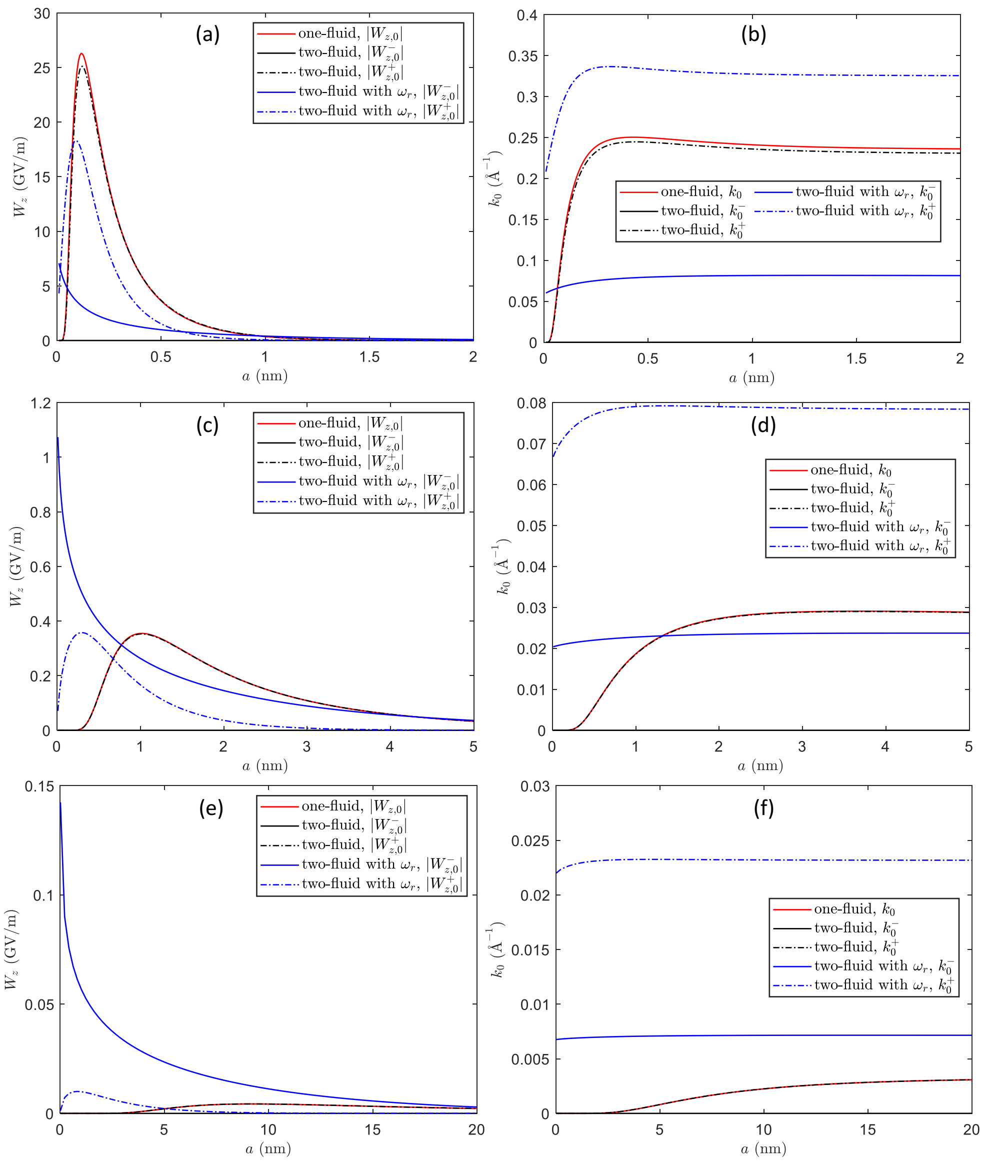


**Figure 10.**
*(a) Amplitudes $W_z$ of the fundamental mode $m = 0$ and (b) corresponding resonant wavenumbers $k_0$ as functions of the CNT radius, computed using the one-fluid model, the standard two-fluid model, and the two-fluid model with restoring frequencies with $\omega_{r\pi} = 4$ eV and $\omega_{r\sigma} = 13$ eV for $v = 0.035$c. (c) and (d), and (e) and (f) are identical to (a) and (b), respectively, but for $v = 0.1$c and $v = 0.3$c, respectively. A value of $r = r_0 = 0$ is considered in all plots.*

### 3.4 Stopping power

Finally, we examine the stopping power $S$, defined as the energy dissipated per unit length by a channelled particle due to collective excitations of electrons along the walls of the nanotube. This quantity can be evaluated through the expression:

$$S = -Q\,W_{z,\,\text{ind}}\big|_{\mathbf{r}=\mathbf{r}_0} = -Q\,W_{z,\,\text{Im}}\big|_{\mathbf{r}=\mathbf{r}_0}. \tag{33}$$

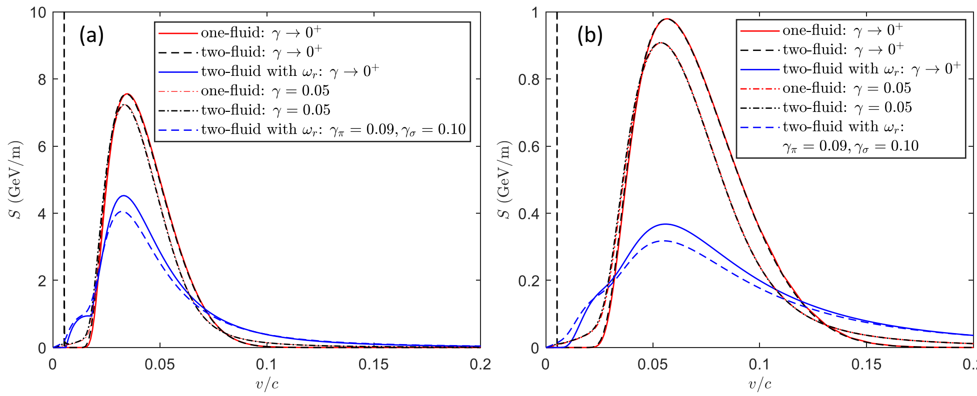


**Figure 11.**
*Stopping power for different damping parameters for the one-fluid model, the two-fluid model, and the two-fluid model with restoring frequencies $\omega_{r\pi} = 4$ eV and $\omega_{r\sigma} = 13$ eV for a positively charged ion ($Q = 1$) travelling on axis ($r_0 = 0$) within a CNT with radius (a) $a = 0.36$ nm and (b) $a = 1$ nm.*

In the limit of vanishing damping, $S$ reduces to a direct summation of the contributions from the excited modes, as described by Eq. (22).

**Figure 11** depicts the stopping power computed for various models under distinct damping parameters for a CNT with $a = 0.36$ nm. It can be observed that as the damping parameter increases, the stopping power decreases and broadens, particularly in the case where realistic values of the damping parameter have been employed.

## 4. Concluding remarks

We have revisited the LHM to obtain analytical expressions for the electric wakefields induced by a charged particle propagating paraxially to a CNT. Three variants of the hydrodynamic model have been discussed: the one-fluid model; the two-fluid model, which distinguishes between $\pi$ and $\sigma$ electrons; and the extended two-fluid hydrodynamic model, which incorporates finite restoring frequencies and is able to accurately capture the experimentally observed dispersion relations. Across all scenarios, closed-form solutions have been obtained under the assumption of weak damping, establishing a direct correspondence with the resonant wavenumbers inferred from the associated dispersion relations.

The influence of driving velocity and CNT radius has been analyzed, revealing that both the one-fluid and two-fluid models produce comparable outcomes, except when the driving velocity approaches the phase velocity $v_p$. In contrast, the predictions obtained using the extended two-fluid model differ significantly, as two distinct modes with different frequencies are generally excited. Consequently, the wakefield pattern does not exhibit a sinusoidal behaviour, which would complicate the injection of a witness beam intended for eventual acceleration. Moreover, the excited wakefields generally possess lower amplitudes compared to those predicted by models that do not incorporate restoring frequencies.

Thus, the effect of restoring frequencies may play a significant role in modeling wakefield excitation in CNTs. Furthermore, this extended model predicts the generation of ultra-high accelerating gradients, in agreement with both one-fluid and two-fluid model predictions, thereby confirming the potential of CNTs as a viable, although extremely challenging, candidate for particle acceleration and the production of ultra-brilliant X-ray radiation sources [55, 56].

## Acknowledgments

This research has received funding from the Ministerio de Universidades (Gobierno de España) through grant FPU20/04958, as well as from the Generalitat Valenciana through grant CIDEGENT/2019/058.

## Abbreviations

| | |
|---|---|
| CNT | Carbon nanotube |
| EELS | Electron energy loss spectroscopy |
| FB | Fourier–Bessel |
| LHM | Linearized hydrodynamic model |
| RF | Radiofrequency |
| SWCNT | Single-walled carbon nanotubes |

## Author details

Pablo Martín-Luna[1*†] and Javier Resta-López[2†]

1 Instituto de Física Corpuscular (IFIC), CSIC-Universitat de València, Spain

2 Instituto de Ciencia de los Materiales (ICMUV), Universidad de Valencia, Valencia, Spain

† These authors contributed equally.

*Address all correspondence to: pablo.martin@uv.es

## References

[1] Abe T, Kageyama T, Sakai H, Takeuchi Y, Yoshino K. Breakdown study based on direct in situ observation of inner surfaces of an rf accelerating cavity during a high-gradient test. Physical Review Accelerators and Beams. 2016; **19**:102001. DOI: 10.1103/ PhysRevAccelBeams.19.102001

[2] Shao J Investigations on rf breakdown phenomenon in high gradient accelerating structures. Springer; 2018. Available from: https:// link.springer.com/book/10.1007/978-98 1-10-7926-9 [Accessed: 2025- November-21]

[3] Thompson MC, Badakov H, Cook AM, Rosenzweig JB, Tikhoplav R, Travish G, et al. Breakdown limits on gigavolt-per-meter electron-beam-driven wakefields in dielectric structures. Physical Review Letters. 2008;**100**:214801. DOI: 10.1103/ PhysRevLett.100.214801

[4] Breuer J, Hommelhoff P. Laser-based acceleration of nonrelativistic electrons at a dielectric structure. Physical Review Letters. 2013;**111**:134803. DOI: 10.1103/ PhysRevLett.111.134803

[5] Peralta E, Soong K, England R, Colby E, Wu Z, Montazeri B, et al. Demonstration of electron acceleration in a laser-driven dielectric microstructure. Nature. 2013;**503** (7474):91–94. DOI: 10.1038/ nature12664

[6] England RJ, Noble RJ, Bane K, Dowell DH, Ng CK, Spencer JE, et al. Dielectric laser accelerators. Reviews of Modern Physics. 2014;**86**:1337–1389. DOI: 10.1103/RevModPhys.86.1337 [Accessed: 2025-November-21]

[7] O'Shea B, Andonian G, Barber S, Fitzmorris K, Hakimi S, Harrison J, et al. Observation of acceleration and deceleration in gigaelectron-volt-per-metre gradient dielectric wakefield accelerators. Nature Communications. 2016;**7**(1):1–7. DOI: 10.1038/ ncomms12763

[8] Tajima T, Dawson JM. Laser electron accelerator. Physical Review Letters. 1979;**43**:267–270. DOI: 10.1103/ PhysRevLett.43.267

[9] Chen P, Dawson JM, Huff RW, Katsouleas T. Acceleration of electrons by the interaction of a bunched electron beam with a plasma. Physical Review Letters. 1985;**54**:693–696. DOI: 10.1103/ PhysRevLett.54.693 [Accessed: 2025- November-21]

[10] Gordon D, Tzeng KC, Clayton CE, Dangor AE, Malka V, Marsh KA, et al. Observation of electron energies beyond the linear dephasing limit from a laser-excited relativistic plasma wave. Physical Review Letters. 1998;**80**:2133–2136

[11] Leemans WP, Nagler B, Gonsalves AJ, Tóth C, Nakamura K, Geddes CG, et al. GeV electron beams from a centimetre-scale accelerator. Nature Physics. 2006;**2**(10):696–699. DOI: 10.1038/nphys418

[12] Litos M, Adli E, An W, Clarke C, Clayton C, Corde S, et al. High-efficiency acceleration of an electron beam in a plasma wakefield accelerator. Nature. 2014;**515**(7525):92–95. DOI: 10. 1038/nature13882

[13] Tajima T, Cavenago M. Crystal x-ray accelerator. Physical Review Letters. 1987;**59**:1440–1443. DOI: 10.1103/PhysRevLett.59.1440

[14] Chen P, Noble RJ A solid state accelerator. In: AIP Conference Proceedings. vol. **156**; 1987. p. 222–227. DOI: 10.1063/1.36458.

[15] Chen P, Noble RJ Crystal channel collider: Ultra-high energy and luminosity in the next century. In: AIP Conference Proceedings. vol. **398**; 1997. p. 273–285. DOI: 10.1063/1.53055.

[16] Borrmann G. Die absorption von röntgenstrahlen im fall der interferenz. Zeitschrift Fur Physik. 1950;**127**(4): 297–323. DOI: 10.1007/BF01329828

[17] Campbell H. X-ray absorption in a crystal set at the bragg angle. Journal of Applied Physics. 1951;**22**(9): 1139–1142. DOI: 10.1063/1.1700122

[18] Zhu Z, Zhu D, Lu R, Xu Z, Zhang W, Xia H The experimental progress in studying of channeling of charged particles along nanostructure. In: Dabagov SB, editor. International Conference on Charged and Neutral Particles Channeling Phenomena. vol. 5974 of Society of Photo-Optical Instrumentation Engineers (SPIE) Conference Series; 2006. p. 382–389. DOI: 10.1117/12.640101.

[19] Chai G, Heinrich H, Chow L, Schenkel T. Electron transport through single carbon nanotubes. Applied Physics Letters. 2007;**91**(10):103101. DOI: 10.1063/1.2778551

[20] Biryukov VM, Bellucci S. Nanotube diameter optimal for channeling of high-energy particle beam. Physics Letters B. 2002;**542**(1):111–115. DOI: 10.1016/S0370-2693(02)02276-1 [Accessed: 2025-November-21]

[21] Bellucci S, Biryukov VM, Cordelli A. Channeling of high-energy particles in a multi-wall nanotube. Physics Letters B. 2005;**608**(1):53–58. DOI: 10.1016/j.physletb.2005.01.003 [Accessed: 2025-November-21]

[22] Bonatto A, Xia G, Apsimon O, Bontoiu C, Kukstas E, Rodin V, et al. Exploring ultra-high-intensity wakefields in carbon nanotube arrays: An effective plasma-density approach. Physics of Plasmas. 2023;**30**(3):033105. DOI: 10.1063/5.0134960

[23] Martín-Luna P, Bonatto A, Bontoiu C, Xia G, Resta-López J. Excitation of wakefields in carbon nanotubes: A hydrodynamic model approach. New Journal of Physics. 2023;**25**(12):123029. DOI: 10.1088/1367-2630/ad127c

[24] Bontoiu C, Apsimon O, Kukstas E, Rodin V, Yadav M, Welsch C, et al. TeV/m catapult acceleration of electrons in graphene layers. Scientific Reports. 2023;**13**:1330

[25] Martín-Luna P, Bonatto A, Bontoiu C, Xia G, Resta-López J Plasmonic excitations in double-walled carbon nanotubes Results in Physics. 2024;**60**:107698. DOI: 10.1016/j.rinp.2024.107698

[26] Martín-Luna P, Resta-López J. Excitation of plasmonic wakefields in multi-walled carbon nanotubes: A hydrodynamic approach. In Kuznetsov DA, editor. Carbon Nanotubes - Recent Advances, Perspectives and Applications. Rijeka: IntechOpen; 2024. DOI: 10.5772/intechopen.114270 [Accessed: 2025-November-21]

[27] Martín-Luna P, Bonatto A, Bontoiu C, Xia G, Resta-López J. Plasmonic excitations in carbon nanotubes: PIC simulations vs hydrodynamic model. In Baccouch M, editor. Computational Fluid Dynamics. Rijeka: IntechOpen; 2024. DOI: 10.5772/intechopen.1006820 [Accessed: 2025-November-21]

[28] Martín-Luna P, Resta-López J. Plasmonic Excitations in Carbon Nanostructures: Carbon Nanotubes Vs. Graphene. In Wang DC, editor. Electromagnetic Field - from Atomic Level to Engineering Applications. Rijeka: IntechOpen; 2025. DOI: 10.5772/intechopen.1009673 [Accessed: 2025-November-21]

[29] Martín-Luna P, Bonatto A, Bontoiu C, Lei B, Xia G, Resta-López J. Wakefield excitation and stopping power in multi-walled carbon nanotubes: One- and two-fluid model. Journal of Physics D: Applied Physics. 2025;**58**(22):225203. DOI: 10.1088/1361-6463/add545

[30] Martín-Luna P, Bonatto A, Bontoiu C, Lei B, Xia G, Resta-López J. Plasmonic excitations in graphene layers. Chinese Journal of Physics. 2025;**97**:607–624. DOI: 10.1016/j.cjph.2025.03.030

[31] Lei B, Zhang H, Bontoiu C, Bonatto A, Martín-Luna P, Liu B, et al. Leaky surface plasmon-based wakefield acceleration in nanostructured carbon nanotubes. Plasma Physics and Controlled Fusion. 2025;**67**(6):065036. DOI: 10.1088/1361-6587/ade00a

[32] Arista NR. Interaction of ions and molecules with surface modes in cylindrical channels in solids. Physical Review A. 2001;**64**:032901. DOI: 10.1103/PhysRevA.64.032901

[33] Arista NR, Fuentes MA. Interaction of charged particles with surface plasmons in cylindrical channels in solids. Physical Review B. 2001;**63**:165401. DOI: 10.1103/PhysRevB.63.165401

[34] Wang YN, Mišković ZL. Energy loss of charged particles moving in cylindrical tubules. Physical Review A. 2002;**66**:042904. DOI: 10.1103/PhysRevA.66.042904

[35] Stöckli T, Bonard JM, Châtelain A, Wang ZL, Stadelmann P. Collective oscillations in a single-wall carbon nanotube excited by fast electrons. Physical Review B. 2001;**64**:115424. DOI: 10.1103/PhysRevB.64.115424

[36] Wang YN, Mišković ZL. Interactions of fast ions with carbon nanotubes: Self-energy and stopping power. Physical Review A. 2004;**69**:022901. DOI: 10.1103/PhysRevA.69.022901

[37] Mowbray DJ, Mišković ZL, Goodman FO, Wang YN. Wake effect in interactions of fast ions with carbon nanotubes. Physics Letters A. 2004;**329**(1):94–99. DOI : 10.1016/j.physleta.2004.06.090 [Accessed: 2025-November-21]

[38] Mowbray DJ, Chung S, Mišković ZL, Goodman FO, Wang YN. Dynamic interactions of fast ions with carbon nanotubes. Nuclear Instruments and Methods in Physics Research Section B: Beam Interactions with Materials and Atoms. 2005;**230**(1):142–147. Atomic Collisions in Solids. DOI: 10.1016/j.nimb.2004.12.032 [Accessed: 2025-November-21]

[39] Mowbray DJ, Mišković ZL, Goodman FO, Wang YN. Interactions of fast ions with carbon nanotubes:

Two-fluid model. Physical Review B. 2004;**70**:195418. DOI: 10.1103/PhysRevB.70.195418

[40] Chung S, Mowbray DJ, Mišković ZL, Goodman FO, Wang YN. Dynamic interactions of fast ions with multiwalled carbon nanotubes. Radiation Physics and Chemistry. 2007;**76**(3):524–528. Proceedings of the 3rd International Conference on Elementary Processes in Atomic Systems. Available from: https://www.sciencedirect.com/science/article/pii/S0969806X06004403.

[41] Wei L, Wang YN. Quantum ion-acoustic waves in single-walled carbon nanotubes studied with a quantum hydrodynamic model. Physical Review B. 2007;**75**:193407. DOI: 10.1103/PhysRevB.75.193407

[42] Song YH, Zhao D, Wang YN. Kinetic study on self-energy and stopping power of charged particles moving in metallic carbon nanotubes. Physical Review A. 2008;**78**:012901. DOI: 10.1103/PhysRevA.78.012901 [Accessed: 2025-November-21]

[43] Zhao D, Song YH, Wang YN. Kinetic Study on Channelling of Protons in Metallic Carbon Nanotubes. Chinese Physics Letters. 2008;**25**(7):2588. DOI: 10.1088/0256-307X/25/7/070

[44] You SY, Song YH, Wang YN. Channeling of protons in double-walled carbon nanotubes in kinetic model. Nuclear Instruments and Methods in Physics Research Section B: Beam Interactions with Materials and Atoms. 2009;**267**(18):3133–3136. Proceedings of the Ninth International Conference on Computer Simulation of Radiation Effects in Solids. Available from: https://www.sciencedirect.com/science/article/pii/S0168583X09007381.

[45] Zhang YY, Sun JZ, Song YH, Mišković ZL, Wang YN. Channeling of protons in single-walled carbon nano tubes based on kinetic and molecular-dynamics treatment. Carbon. 2014;**71**: 196–205. DOI: 10.1016/j.carbon.2014.01.030 [Accessed: 2025-November-21]

[46] Zhang YY, Song YH, Radović I, Wang YN, Mišković ZL. Interactions of moving charged particles with triple-walled carbon nanotubes. The European Physical Journal D. 2017;**71**:219. DOI: 10.1140/epjd/e2017-70744-3

[47] Karbunar L, Borka D, Radović I. Image potential and stopping force in the interaction of fast ions with carbon nanotubes: The extended two-fluid hydrodynamic model. Nuclear Instruments and Methods in Physics Research Section B: Beam Interactions with Materials and Atoms. 2016;**366**:83–89. DOI: 10.1016/j.nimb.2015.10.033

[48] Moslem WM, El-Said AS, Tolba RE, Bahlouli H. Modifications of single walled carbon nanotubes by ion-induced plasma. Results in Physics. 2022;**37**:105438. DOI: 10.1016/j.rinp.2022.105438

[49] Östling D, Tománek D, Rosén A. Electronic structure of single-wall, multiwall, and filled carbon nanotubes. Physical Review B. 1997;**55**:13980–13988. DOI: 10.1103/PhysRevB.55.13980

[50] Hakimi S, Nguyen T, Farinella D, Lau CK, Wang HY, Taborek P, et al. Wakefield in solid state plasma with the ionic lattice force. Physics of Plasmas. 2018;**25**(2):023112. DOI: 10.1063/1.5016445

[51] Hakimi S, Zhang X, Lau C, Taborek P, Dollar F, Tajima T. X-ray laser wakefield acceleration in a

nanotube. International Journal of Modern Physics A. 2019;**34**(34):1943011. DOI: 10.1142/S0217751X19430115

[52] Nejati M, Javaherian C, Shokri B, Jazi B. The single-wall carbon nanotube waveguides and excitation of their plasmons by an electron beam. Physics of Plasmas. 2009;**16**(2):022108. DOI: 10.1063/1.3077306

[53] Mowbray DJ, Segui S, Gervasoni J, Mišković ZL, Arista NR. Plasmon excitations on a single-wall carbon nanotube by external charges: Two-dimensional two-fluid hydrodynamic model. Physical Review B. 2010;**82**:035405. DOI: 10.1103/PhysRevB.82.035405

[54] Jovanović VB, Radović I, Borka D, Mišković ZL. High-energy plasmon spectroscopy of freestanding multilayer graphene. Physical Review B. 2011;**84**:155416. DOI: 10.1103/PhysRevB.84.155416

[55] Shin YM. Optically controlled coherent X-ray radiations from photo-excited nanotubes. Nuclear Instruments and Methods in Physics Research Section B: Beam Interactions with Materials and Atoms. 2017;**407**:276–281. DOI: 10.1016/j.nimb.2017.07.019 [Accessed: 2025-November-21]

[56] Shou Y, Wang P, Lee SG, Rhee YJ, Lee HW, Yoon JW, et al. Brilliant femtosecond-laser-driven hard X-ray flashes from carbon nanotube plasma. Nature Photonics. 2023;**17**:137–142